Journal of Advanced Ceramics
2016, **5**(1): 54–69
DOI: 10.1007/s40145-015-0173-x

ISSN 2226-4108
CN 10-1154/TQ

Research Article

Electrical and mechanical properties of (Bi,Pb)-2223 substituted by holmium

W. ABDEEN[a,b,*], S. MARAHBA[c], R. AWAD[c], A. I. ABOU ALY[a], I. H. IBRAHIM[a], M. MATAR[a]

[a]*Superconductivity and Metallic Glass Lab*, *Physics Department*, *Faculty of Science*, *Alexandria University*, *Alexandria*, *Egypt*
[b]*Physics Department*, *University College at Al-Gamom*, *Umm Al-Qura University*, *Saudi Arabia*
[c]*Physics Department*, *Faculty of Science*, *Beirut Arab University* (*BAU*), *Beirut*, *Lebanon*

Received: August 30, 2015; Revised: October 14, 2015; Accepted: October 15, 2015

Abstract: The effect of the partial substitution of Ca^{2+} by Ho^{3+} ions on the electrical and mechanical properties of the superconducting phase (Bi,Pb)-2223 was studied. Superconducting samples of the type $(Bi_{1.8}Pb_{0.4})Sr_2Ca_{2.1-x}Ho_xCu_{3.1}O_{10+\delta}$ were prepared by solid-state reaction technique under ambient pressure, and characterized by means of X-ray powder diffraction (XRD) and scanning electron microscopy (SEM). The superconducting transition temperature T_c and pseudogap temperature T^* were estimated from electrical resistivity measurements, while the critical current density J_c was determined from *I–V* curves. The electrical resistivity data were discussed according to bipolaron model in the absence of thermally excited individual polarons. The sample with $x = 0.025$ showed the highest phase volume fraction, T_c, and J_c. Room temperature Vickers microhardness measurements were carried out at different applied loads (0.25–5 N) in order to investigate the performance of the mechanical properties of $(Bi_{1.8}Pb_{0.4})Sr_2Ca_{2.1-x}Ho_xCu_{3.1}O_{10+\delta}$ phase. It was found that all the samples exhibit normal indentation size effect (ISE). The Vickers microhardness number H_V increased as x increased from 0 to 0.025. The experimental results were discussed in view of Meyer's law, Hays–Kendall (HK) approach, elastic/plastic deformation (EPD) model, and proportional specimen resistance (PSR) model. The load independent (true) microhardness of $(Bi_{1.8}Pb_{0.4})Sr_2Ca_{2.1-x}Ho_xCu_{3.1}O_{10+\delta}$ superconducting samples showed identical behavior to that of the PSR model.

Keywords: (Bi,Pb)-2223 phase; Ho substitution; Vickers microhardness; bipolaron model; pesudogap temperature

1 Introduction

(Bi,Pb)-2223 phase is the most promising one among the bismuth strontium calcium copper oxide (BSCCO) system to synthesize tapes and wires for large scale and high current applications, owing to its high superconducting transition temperature T_c and favorable characteristics such as atmospheric stability, high current and magnetic field carrying capacity, and electronic properties in view of a possible use in superconducting devices operated at liquid nitrogen temperature [1]. On the other hand, there are some

* Corresponding author.
E-mail: waleed_abdeen@alex-sci.edu.eg

problems which limit the practical applications of (Bi,Pb)-2223; the most limiting parameters for the practical applications of this phase are critical current density J_c and mechanical properties [2]. Since the discovery of high temperature superconductors (HTSCs), many substitutions have been carried out in BSCCO system in order to improve its T_c and J_c, and better understand the structural, physical, and mechanical properties [3–8]. The rare-earth element chemical substitution has an effective route in improving the flux pinning centers, which in turn enhance J_c and other transport properties of (Bi,Pb)-2223 phase [9]. The partial substitution of Ca^{2+} ions by rare-earth element R^{3+} ions on the (Bi,Pb)-2223 phase has a significant effect on its normal and superconducting properties [10]. The previous studies showed that T_c values are gradually decreased with the increase of R^{3+} content [10–15]. The effect of partial substitution of Sm and Eu at Ca site in (Bi,Pb)-2223 system on the superconducting, microstructure, and mechanical properties was studied [12–16]. It was found that the volume fraction of (Bi,Pb)-2223 phase decreases with increasing Sm content. Moreover, the superconducting properties and mechanical properties degrade with increasing Sm content. Also, J_c decreases by increasing Eu content and this decrease is related to the weakness of the grain connectivity and the increment of the porosity for (Bi,Pb)-2223 phase. In addition, the lattice parameter *c* decreases and the crystallographic structure is found to change slightly from tetragonal to orthorhombic.

The normal state properties of HTSCs, especially the metallic like behavior of electrical resistivity, can be discussed according to the bipolaron model [17]. Bipolarons could be created by the interaction between holes and optical phonons in HTSCs. Alexandrov and Mott [18] reported that for a system with large electron–phonon coupling constant, a Bose condensation of bipolarons can take place in the real space. Due to the extremely short coherence length of HTSCs, a cross-over region from Bardeen–Cooper–Schrieffer (BCS) to Bose–Einstein condensation (BEC) superfluids is considered in some theoretical studies related to their pairing mechanism. In the bipolaron model, however, BEC is only considered as paired state [19]. The bipolaron model is sensitive to both substitution concentration and sample crystal structure [20,21].

The understanding of normal state properties of HTSCs would provide important evidences about the basic mechanisms responsible for superconductivity in HTSCs. Thus, the normal state properties of HTSCs remain an area of intense research. One of the clearest differences between the BCS scenario of superconductivity and high T_c cuprates is the existence of a pseudogap. According to the band theory representation, pseudogap refers to some gapped regions in the Fermi surface, while other parts retain their conducting character. The chemical substitution changes the gapped region and metallicity of the material. The pseudogap is a fundamental property of the under-doped copper oxides, where the presence of pseudogap leads to striking deviation of resistivity from simple linear behavior [22–25]. However, the temperature dependence of resistivity for under-doped HTSCs shows a distinguishable deviation from linear behavior at the pseudogap temperature T^*. The recent literature indicated that, there are two scenarios for the explanation of the pseudogap temperature in HTSCs. According to the first scenario, pseudogap is related to short-range ordering fluctuations, e.g., antiferromagnetic fluctuations, spin, and charge density waves, etc. [22]. The second scenario assumes that Cooper pairs are formed at temperatures much higher than T_c; $T^* > T_c$, and further phase coherence realizes at $T < T_c$ [26,27].

The mechanical properties of small size samples can be measured using Vickers indentation method [28–31]. The effect of chemical substitution/addition on Vickers microhardness for (Bi,Pb)-2223 phase was studied by many groups [12–15,32–34]. It was found that the substitution of Sm at Ca site increases H_V due to the enhancement in grain connectivity, and the modified proportional specimen resistance model was found to be the most successful model describing the load independent microhardness [32]. Addition of Gd^{3+} ions to (Bi,Pb)-2223 degrades the mechanical properties [33,34]. This degradation is related to the increase of voids, impurity phase segregation, and the modification of the grain boundaries.

In this work, we present a detailed study of the effect of Ho^{3+} substitution at Ca^{2+} site in (Bi,Pb)-2223 phase. This study includes X-ray powder diffraction (XRD), scanning electron microscopy (SEM), electrical resistivity, *I–V* characteristics, and Vickers microhardness for $(Bi_{1.8}Pb_{0.4})Sr_2Ca_{2.1-x}Ho_xCu_{3.1}O_{10+\delta}$ samples with $0.000 \leqslant x \leqslant 0.200$.

2 Experimental details

Conventional solid-state reaction technique was

used to prepare superconducting samples of $(Bi_{1.8}Pb_{0.4})Sr_2Ca_{2.1-x}Ho_xCu_{3.1}O_{10+\delta}$ with $0.000 \leqslant x \leqslant 0.200$. The starting materials were Bi_2O_3, PbO, PbO_2, $SrCO_3$, CaO, CuO, and Ho_2O_3 (purity ⩾ 99.9%, Sigma-Aldrich). The stoichiometric mixture of the starting materials was ground manually in an agate mortar and sifted using a 65 μm sieve. Then, the resulting powder was subjected to two stages of calcinations in air at 820 ℃ for 24 h for each with intermediate grinding and sieving. This is important to obtain the proper precursor phases necessary for the formation of (Bi,Pb)-2223. The phase assemblage is sensitive to the calcination conditions [35]. After that, the mixture was cooled to room temperature and then ground and sifted. Then, the powder was pelletized into a disc with diameter of 1.5 cm and thickness of about 0.3 cm at a pressure of 15 tons/cm^2. The pellets were sintered in air (atmospheric pressure) at 845 ℃ for 96 h with a heating rate of 4 ℃/min, and they were cooled with a rate of 2 ℃/min to room temperature. After that, the sintered samples were ground, sifted, and then pressed again in the form of disc and re-sintered in air at 845 ℃ for 48 h with a heating rate of 2 ℃/min. Finally, the samples were cooled with a rate of 1 ℃/min to room temperature.

The prepared samples were characterized by XRD using a Philips X'Pert powder diffractometer with Cu Kα radiation ($\lambda = 1.54056$ Å) in the range of $4° \leqslant 2\theta \leqslant 70°$. The grain size and morphology of the samples' surface were identified using a Jeol scanning electron microscope JSM-5300, operated at 30 kV, with a resolution power of 4 nm.

The electric resistivity of the prepared samples was measured by the conventional four-probe technique from room temperature down to zero resistivity temperature T_0 via a closed cryogenic refrigeration system (Displex) employing helium gas as a working medium. The transport critical current density was measured by the conventional four-probe technique at 77 K in a flow of liquid nitrogen using the standard 1 μV/cm criterion. The temperature of the samples was monitored by Fe–Au thermocouple and stabilized with the aid of a temperature controller within ±0.1 K.

Vickers microhardness measurements of the studied samples were performed in atmospheric air at room temperature using a manual microhardness tester IN-412A. A Vickers pyramidal indenter with different applied loads varied from 0.25 to 5.00 N and a loading time of 10 s was used to measure the diagonals of indentation with an accuracy of ±0.1 μm. An average of 7 readings at different locations of specimen surface was taken to obtain sensible mean value for each load. The measurements were carried out in such a way that the distance between any two indentations was more than two times the diagonal of the indentation mark to avoid surface effects due to neighboring indentation. The Vickers microhardness is defined as the ratio of applied load to the pyramidal contact area of indentation, and it is calculated as [36]:

$$H_V = 1854.4\frac{F}{d^2} \quad (1)$$

where F is the applied load (N) and d is the diagonal length of the indentation mark (μm).

3 Results and discussion

3.1 Characterization and investigation

The XRD patterns for $(Bi_{1.8}Pb_{0.4})Sr_2Ca_{2.1-x}Ho_xCu_{3.1}O_{10+\delta}$ samples with $x = 0.000$, 0.025, 0.075, and 0.200 at room temperature are shown in Fig. 1. It is observed that most of the high-intensity peaks belong to tetragonal phase of (Bi,Pb)-2223 with a space group *P*4/*mmm* [37]. There are a few low-intensity peaks belonging to other phases, such as (Bi,Pb)-2212 and Ca_2PbO_4. These impurity phases are typically observed in the preparation of (Bi,Pb)-2223 by solid-state reaction technique [10,35,37–39]. The notations "*" and "+" indicate the peaks of (Bi,Pb)-2212 and Ca_2PbO_4, respectively. The characteristic peak intensity of (Bi,Pb)-2223 phase (002) increases as x increases from 0.000 to 0.025, indicating that the low content of Ho can enhance the phase formation of

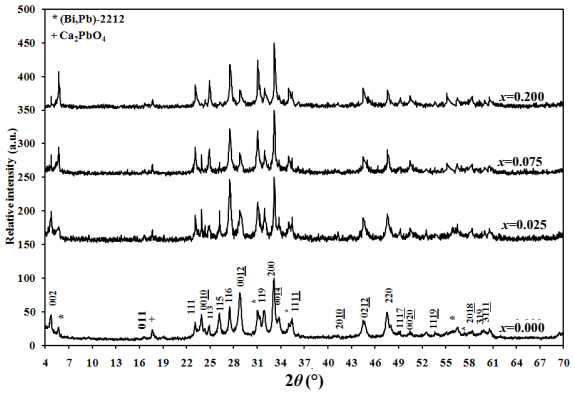

Fig. 1 XRD patterns for $(Bi_{1.8}Pb_{0.4})Sr_2Ca_{2.1-x}Ho_xCu_{3.1}O_{10+\delta}$ samples with $x = 0.000$, 0.025, 0.075, and 0.200 at room temperature.

(Bi,Pb)-2223 phase. For $x > 0.025$, the intensity of characteristic peaks of (Bi,Pb)-2223 decreases while the intensity of characteristic peaks of (Bi,Pb)-2212 increases. This means that the high Ho content retards the growth of (Bi,Pb)-2223 phase. Furthermore, no peaks belong to Ho rich compounds observed in the XRD patterns. This means that the Ho ions enter into the crystal structure of (Bi,Pb)-2223. Similar results were reported for (Bi,Pb)-2223/Ag taps substituted by Pr ions at Ca site [40]. This indicates the high solubility limit of Ho in the crystal structure of (Bi,Pb)-2223 phase.

The relative volume fractions of (Bi,Pb)-2223, (Bi,Pb)-2212, and Ca_2PbO_4 phases are calculated using Eqs. (2)–(4), respectively [5,10,28,37], and their values are listed in Table 1 with Ho content.

$$\text{(Bi,Pb)-2223}(\%) = \frac{\sum I_{\text{(Bi,Pb)-2223}}}{\sum I_{\text{(Bi,Pb)-2223}} + \sum I_{\text{(Bi,Pb)-2212}} + \sum I_{Ca_2PbO_4}} \times 100\% \quad (2)$$

$$\text{(Bi,Pb)-2212}(\%) = \frac{\sum I_{\text{(Bi,Pb)-2212}}}{\sum I_{\text{(Bi,Pb)-2223}} + \sum I_{\text{(Bi,Pb)-2212}} + \sum I_{Ca_2PbO_4}} \times 100\% \quad (3)$$

$$Ca_2PbO_4(\%) = \frac{\sum I_{Ca_2PbO_4}}{\sum I_{\text{(Bi,Pb)-2223}} + \sum I_{\text{(Bi,Pb)-2212}} + \sum I_{Ca_2PbO_4}} \times 100\% \quad (4)$$

where I represents the peak intensity of the indicated phases. A little increase in the volume fraction of (Bi,Pb)-2223 phase is observed for $x = 0.025$, and then it decreases for $x > 0.025$, while the volume fraction of low-T_c phase (Bi,Pb)-2212 decreases with $x = 0.025$ and increases for $x > 0.025$. These observations indicate that the low content of holmium enhances the formation of the (Bi,Pb)-2223 phase which could be due to the ability of Ho to provide a suitable medium for the conversion of the (Bi,Pb)-2212 phase to the (Bi,Pb)-2223 phase and reduce the impure phases. While the further increase of x leads to a change in the reaction rate which retards slightly the (Bi,Pb)-2223 formation. A similar behavior was observed in many previous studies, concerning the effect of R^{3+} ions on (Bi,Pb)-2223 phase [11–14].

The lattice parameters a and c were calculated using the least square method through d value and (hkl) planes for tetragonal unit cell structure. Their variations versus Ho content are also listed in Table 1. It is found that the lattice parameters a and c for the un-substituted sample are very close to those obtained by Koyama *et al.* [41] and Abou-Aly *et al.* [42]. Moreover, for all substituted samples, the lattice parameter a increases slightly with increasing Ho content while the lattice parameter c decreases significantly. Similar behavior has been observed in previous works involving substitution of rare-earth elements at Ca site in the (Bi,Pb)-2223 system [10–13,43,44]. This behavior can be explained according to two reasons. The first one is attributed to the partial substitution of larger ionic radius of Ca^{2+} ion, 0.990 Å, by the smaller one of Ho^{3+} ion, 0.901 Å, at the same 6-fold coordination type [45]. The second reason is that the partial substitution of Ca^{2+} ions by Ho^{3+} ions leads to an increase in the oxygen content of the unit cell that enhances the average oxidation state, leading to smaller Cu–O distance within the copper–oxygen sheets [46]. In addition, the lattice parameter a is controlled by the length of the in-plane Cu–O bond which may be expanded as a result of electron addition into anti-bonding orbital through the partial substitution of Ca^{2+} ions by Ho^{3+} ions [47].

Table 1 Variation of the relative volume fraction of (Bi,Pb)-2223, (Bi,Pb)-2212, and Ca_2PbO_4 phases, lattice parameters a and c for $(Bi_{1.8}Pb_{0.4})Sr_2Ca_{2.1-x}Ho_xCu_{3.1}O_{10+\delta}$ phase with $0.000 \leqslant x \leqslant 0.200$

x	Relative volume fraction (%)			Lattice parameter (Å)	
	(Bi,Pb)-2223	(Bi,Pb)-2212	Ca_2PbO_4	a	c
0.000	88.16	10.48	1.36	5.397(6)	37.174(4)
0.025	89.89	8.92	1.19	5.399(6)	37.168(8)
0.050	84.86	13.95	1.18	5.400(9)	37.150(3)
0.075	82.58	15.99	1.43	5.401(2)	37.143(6)
0.100	81.42	17.08	1.50	5.401(9)	37.130(2)
0.150	80.75	17.50	1.74	5.402(2)	37.126(0)
0.200	79.50	18.15	2.35	5.402(4)	37.120(1)

The SEM micrographs of the fractured surface of the prepared samples with $x = 0.000$, 0.025, 0.075, and 0.200 are shown in Figs. 2(a)–2(d), respectively. The granular morphology for the un-substituted sample x = 0, consists primly of flaky layers of large platelet-like structure with random alignment distribution as shown in Fig. 2(a), which is a signature of (Bi,Pb)-2223 phase formation [48,49]. The platelet grains are well linked as x increases to 0.025, in which the platelet-like grains still have a flaky structure. Additionally, the sample has more uniform surface appearance with larger average grain size and lower porosity as shown in Fig. 2(b). The average grain size increases from 1.99 to 2.27 μm (calculated from the SEM) as Ho content increases from $x = 0.000$ to $x = 0.025$ and then decreases to 1.06 μm for $x = 0.200$. This indicates that the low Ho content increases the growth of (Bi,Pb)-2223 phase,

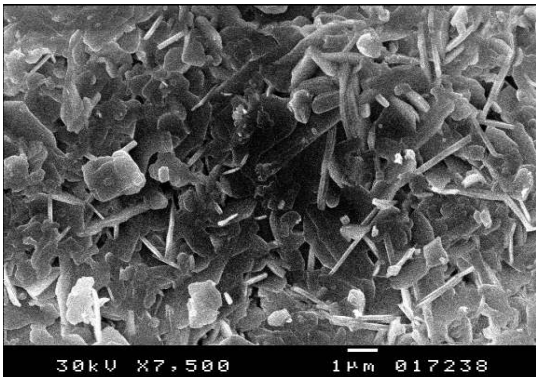

(a)

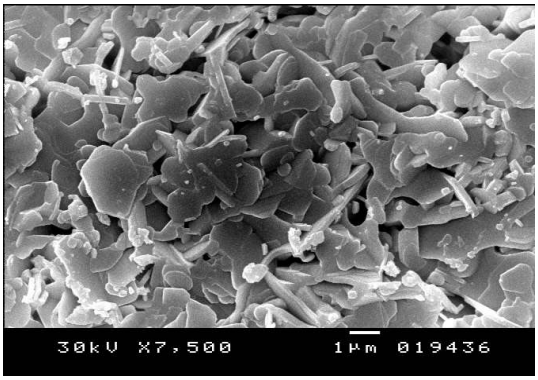

(b)

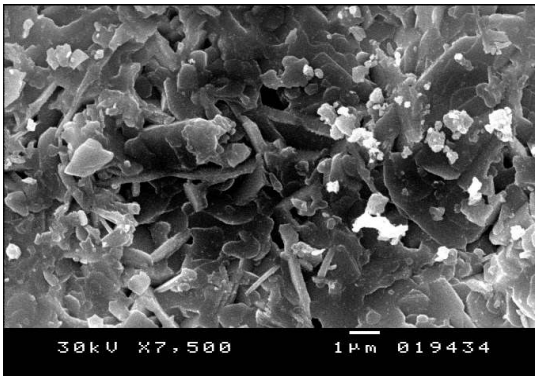

(c)

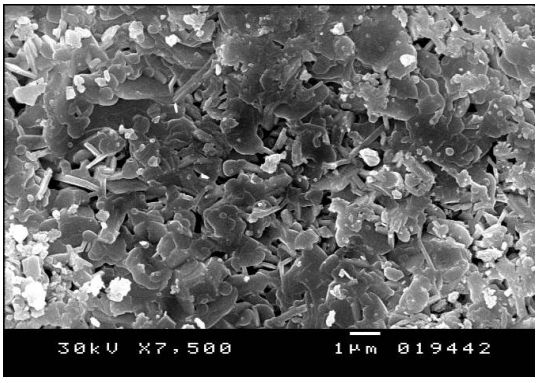

(d)

Fig. 2 SEM images of the fractured surface of the prepared samples $(Bi_{1.8}Pb_{0.4})Sr_2Ca_{2.1-x}Ho_xCu_{3.1}O_{10+\delta}$ with x = (a) 0.000, (b) 0.025, (c) 0.075, and (d) 0.200.

consistent with the enhancement of volume fraction of (Bi,Pb)-2223 phase at low concentration. As the Ho content increases, the platelet shape is not changed, whereas the grain dimensions are changed and oriented randomly. The number of thin rectangular grains increases, indicating the increase in the low-T_c (Bi,Pb)-2212 phase, voids, and hence porosity. Furthermore, the number of spherical grains refers to the Ca_2PbO_4 non-superconducting phase increasing. According to these observations, the surface morphology of the superconducting samples improves with the Ho^{3+} ions in the (Bi,Pb)-2223 phase with x = 0.025. This may lead to the divergence from the optimum doping level and optimization of the hole concentration. Similar result was reported by Anis-ur-Rehman *et al.* [50] substituting Ce^{3+} ions at Ca site in (Bi,Pb)-2223 phase.

The electrical resistivity of the superconducting samples $(Bi_{1.8}Pb_{0.4})Sr_2Ca_{2.1-x}Ho_xCu_{3.1}O_{10+\delta}$ with x = 0.000, 0.025, 0.075, and 0.200 as a function of temperature is shown in Fig. 3. All the prepared samples have a metallic-like behavior at high temperatures followed by a superconducting transition as the temperature is lowered. The normal metallic-like behavior above T_c can be interpreted by the liquid model and it reflects the spin charge separation in CuO_2 planes that results in the longitudinal transport relaxation rate $1/\tau \approx T$ [51]. It is noticed that the electrical resistivity behavior does not show the existence of a secondary phase at higher Ho contents, implying that the samples are mainly single phase. This result is consistent with that obtained through the X-ray investigation. A small curvature in electrical resistivity above T_c is observed for all

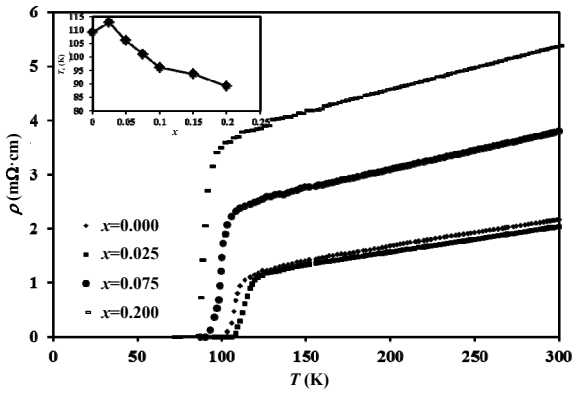

Fig. 3 Temperature dependence of the electrical resistivity for $(Bi_{1.8}Pb_{0.4})Sr_2Ca_{2.1-x}Ho_xCu_{3.1}O_{10+\delta}$ with x = 0.000, 0.025, 0.075, and 0.200. The insert shows the variation of T_c with x.

samples, which characterizes the superconducting thermodynamic fluctuations [52] or the opening of spin-gap that appears in the HTSCs due to magnetic impurity substitutions [53]. These superconducting thermodynamic fluctuations occur at finite temperatures just above T_c due to the appearance of Cooper pairs even above this temperature.

The superconducting transition temperature T_c, which displays the superconducting transition within the grains, is determined as the temperature corresponding to the crest in $d\rho/dT$ versus T curve [54]. The inset in Fig. 3 shows the variation of T_c with x for $(Bi_{1.8}Pb_{0.4})Sr_2Ca_{2.1-x}Ho_xCu_{3.1}O_{10+\delta}$. It is clear that T_c enhances as x increases from 0.000 to 0.025 and then it decreases with the further increase in x. The parabolic dependence of T_c on x is considered to be a typical character of the substituted high temperature superconductors [11]. This relation indicates that the un-substituted sample lies in the under-doped region [12]. The enhancement of T_c can be explained according to the increase in the formation of (Bi,Pb)-2223 and well linked grains for $0.000 < x \leqslant 0.025$. It is also probably due to a change of the average oxidation state of copper as reported by Laximi Narasaiah *et al*. [55] substituting Y^{3+} ions in (Bi,Pb)-2223. They found an increase in T_c at low Y content. There are two different explanations for the strong depression of T_c for $x > 0.025$. The first one due to Abrikosov–Gor'kov theory [56] is related to a Cooper pair breaking mechanism as a result of the magnetic ion substitution, and leads to a disorder in the internal magnetic state. The second one is due to the scattering between the Cooper pair and magnetic ions according to spin-flip process [57]. This process is characterized by total spin conservation in the scattering event, so the spin of Ho atom must flip when the Cooper pairs are broken. The location of carriers can play important role for enhancement or decrement of T_c, which will discuss later by bipolaron model.

To compare our results with different R^{3+} substitution [58–60], the variation of the reduced transition temperature ($T_c(x)/T_c(0)$) with rare-earth elements is plotted in Fig. 4. It is clear that, the critical concentration of Ho^{3+} ions required to destroy the superconductivity of (Bi,Pb)-2223 samples ($x > 0.200$) is higher than that reported for Sm^{3+} ($x = 0.2$), Pr^{3+} ($x = 0.1$), and $Ce^{3+\text{ or }4+}$ ($x = 0.1$) ions [58–60]. This indicates that Ho^{3+} ions have a higher solubility limit in the (Bi,Pb)-2223 phase and are less detrimental to

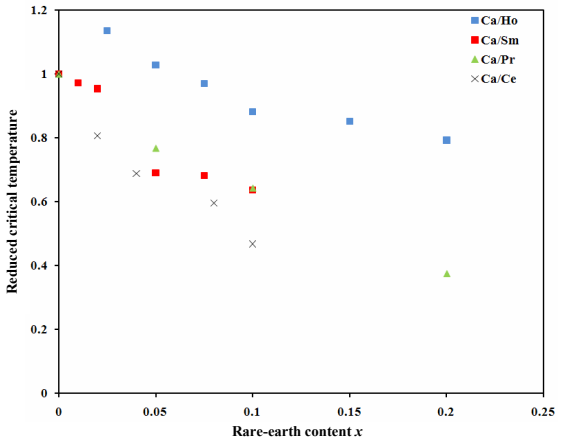

Fig. 4 Reduced critical temperature versus rare-earth content of (Bi,Pb)-2223 samples.

superconductivity. The solubility limit of rare-earth elements R^{3+} in the (Bi,Pb)-2223 phase can be understood by a comparison of their ionic radii of 0.901, 0.958, 0.990, and 1.034 Å for Ho^{3+}, Sm^{3+}, Pr^{3+}, and Ce^{3+}, respectively, with respect to 0.990 Å of Ca^{2+} [45]. This means that the solubility limit may increase as the difference of ionic radii increases [10].

There are only a few models concerning the linear temperature dependence of the electrical resistivity of the HTSCs. One may exclude boson–boson and boson–phonon scatterings which are responsible for linear resistivity behavior at high and low temperatures, respectively [61]. Despite the polycrystalline nature of our samples, the data of electrical resistivity are analyzed using bipolaron model. In the first attempt of bipolaron model, normal state resistivity data are compared with a condition in which the contributions of the thermally excited individual polarons have not been taken into account [62]. This model is based on the localization of carriers by disorders and it predicts a linear behavior for the normal state resistivity. Considering the residual resistivity is zero, the temperature dependence of resistivity is given by Eq. (5):

$$\rho = \left(\frac{m^2 CV}{4e^2}\right)\frac{T + \sigma_b T^2}{N - N_L + bN_L T} \tag{5}$$

where m is the in-plane boson mass; C is a constant proportional to the deformation potential; V is the volume of the elementary cell; N_L is the number of localized states per unit cell; and $bN_L T$ is the density of unoccupied potential wells. $\sigma_b = \alpha e^2 b N_L / (m^2 C)$ is the relative boson–boson scattering cross section in which α is a constant.

The experimental electrical resistivity data and those fitted according to Eq. (5) are plotted in Fig. 5. In this figure, $\rho(T)$ deviates downwards from linear behavior at temperature T^* corresponding to the pseudogap opening [63]. The fitting parameters for different substituted samples are listed in Table 2. The parameter m^2C, which corresponds to the rate of resistivity change, decreases slightly as Ho content x increases to 0.025 and then it increases with further increase in x. The boson–boson scattering cross section can also alter the rate of resistivity change and its value increases by the increase of Ho concentration till $x = 0.025$ and then has reverse trends for $x > 0.025$. The number of localized states decreases slightly by substitution up to $x = 0.025$. The localization of carriers by impurities may also play a useful role to describe T_c increment or suppression. The boson–boson relaxation time is proportional to parameter bN_L as $1/\tau_{b-b} = (\alpha e^2T^2/m)bN_L$ and the increasing of bN_L for our data shows that Ho doping causes a decrease in τ_{b-b} value till $x = 0.025$. A reverse trend is observed for $x > 0.025$.

The T^* value is also determined by analyzing the first derivative $d\rho/dT$ with respect to temperature at finite $d\rho/dT$ [64] as shown in Fig. 6. From the figure we can see that $(d\rho/dT)/(d\rho/dT)_{T=160K}$ reduces as the temperature increases and then converges to a constant value at which T^* can be determined. Table 3 displays the variation of T^* values with x. It is clear that T^* values decrease by increasing Ho content up to $x = 0.100$ and then increase for $x \geqslant 0.150$. This enhancement can be explained by anti-ferromagnetic correlation in the CuO_2 planes according to t–J model or extended t–J model [65], due to Ho substitution. The effective interplane coupling can be strongly enhanced by strong spin anti-ferromagnetic correlation, and extend over a coherence length of several lattice spacing. The enhanced coupling also leads to enhanced pairing between fermions on adjacent planes, thus is responsible for the formation of the spin gap [23]. In addition, it is observed that the values of pseudogap temperature estimated from the deviation of $\rho(T)$ from the linearity and those from the first derivative $d\rho/dT$ with respect to $d\rho/dT$ at finite temperature are nearly close to each others.

The E–J curves for $(Bi_{1.8}Pb_{0.4})Sr_2Ca_{2.1-x}Ho_xCu_{3.1}$

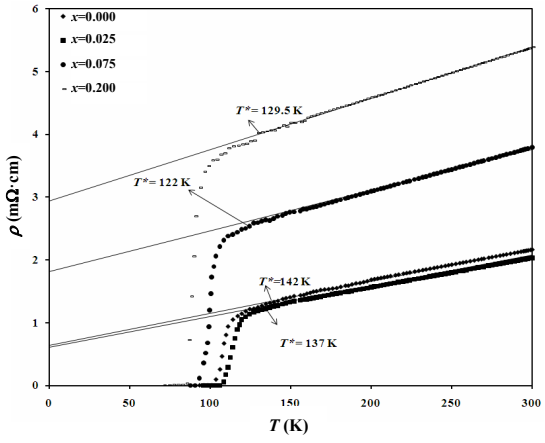

Fig. 5 Resistivity data for $(Bi_{1.8}Pb_{0.4})Sr_2Ca_{2.1-x}Ho_xCu_{3.1}O_{10+\delta}$ with $x = 0.000$, 0.025, 0.075, and 0.200 compared with Eq. (5).

Table 2 Doping dependence of fitting parameters of Eq. (5) obtained from the experimental resistivity data

x	m^2C (10^{-20})	σ_b (10^{-3})	N–N_L (10^{-3})	bN_L ($10^{-4}K^{-1}$)
0.000	75.85	6.38	1.50	9.31
0.025	58.75	7.56	3.07	9.33
0.050	74.16	6.75	2.37	6.88
0.075	85.14	5.77	2.30	6.15
0.100	85.23	3.38	2.15	4.50
0.150	92.45	3.06	1.22	4.13
0.200	92.73	3.04	1.09	3.99

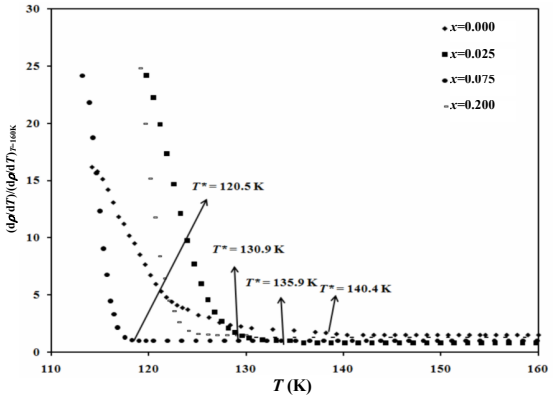

Fig. 6 Variation of $(d\rho/dT)/(d\rho/dT)_{T=160K}$ versus T curves for $(Bi_{1.8}Pb_{0.4})Sr_2Ca_{2.1-x}Ho_xCu_{3.1}O_{10+\delta}$ phase with $x = 0.000$, 0.025, 0.075, and 0.200.

Table 3 Variation of T^* with x for $Bi_{1.8}Pb_{0.4}Sr_2Ca_{2.1-x}Ho_xCu_{3.1}O_{10+\delta}$ phase

x	T^* (K)	
	Estimated from $(d\rho/dT)/(d\rho/dT)_{T=160K}$ independent on temperature	Estimated from deviation $\rho(T)$ from linear behavior
0.000	140.4	142.0
0.025	135.9	137.0
0.050	126.5	124.5
0.075	120.5	122.0
0.100	110.7	111.0
0.150	118.9	122.0
0.200	130.9	129.5

$O_{10+\delta}$ with $x=0.000$, 0.025, 0.075, and 0.200 are shown in Fig. 7. The explanation of these curves can be divided into four parts as follows: (1) The system is resistanceless, $V(I)=0$, when the current is not large enough to cause vortex pair unbinding [66]. (2) At very low values of voltage, the linear E–J behavior can be discussed according to the thermally assisted flux flow (TAFF) as the free vortices are created below T_c as a result of a finite penetration depth [67]. (3) In the non-linear behavior, the voltage drop appears at certain value of applied current I_c, and this part can be understood as a result of the equality of Lorentz force and the pinning force, $F_L=F_p$. Therefore, one can expect to see flux creep due to the weak link junctions that impede the flux motion. (4) In the last linear region in the E–J characteristic curve, the magnitude of the current increases and the Lorentz force is strong enough to cause vortex pair unbinding. So, this linear region in the E–J characteristic curve can be discussed according to the flux flow which occurs at high values of applied current or high values of applied magnetic fields in which $F_L>F_p$ [68,69]. The variation of J_c for $(Bi_{1.8}Pb_{0.4})Sr_2Ca_{2.1-x}Ho_xCu_{3.1}O_{10+\delta}$ with $0.000\leqslant x\leqslant 0.200$ is shown in the inset in Fig. 7. It is clear that the J_c values increase as Ho content increases from $x=0.000$ to $x=0.025$, and then decrease with further increase in x. The increase in J_c is related to the enhancement in the volume fraction of (Bi,Pb)-2223, or the improving of grain boundaries. A similar result was observed by Pu *et al.* [40] when they substituted Pr^{3+} ions at Ca site with very small percentages in (Bi,Pb)-2223/Ag tapes. On the other hand, the formation of (Bi,Pb)-2212 increases with $x>0.025$ and could be residual at the grain boundaries. This decreases the intergranular Josephson coupling energy and hence decreases of the pinning of intergranular vortices [70]. Thus, one can contribute the decrease in T_c and J_c with increasing Ho content to the suppression of the relative volume fraction for (Bi,Pb)-2223 phase and the growth of the impurity content, as well as the increase in porosity accompanied with the increase in grain boundary weak links. This result is in consistent with the XRD data.

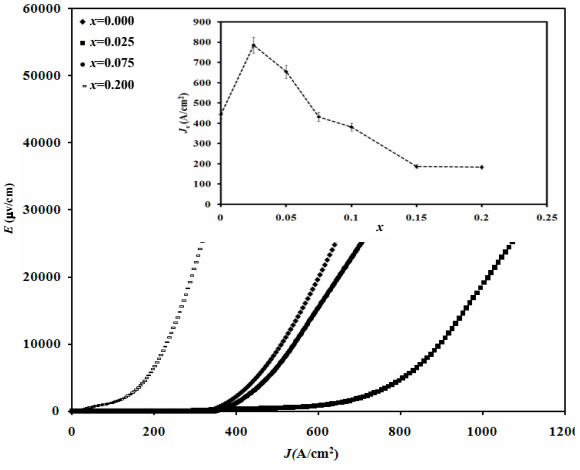

Fig. 7 E–J curves for $(Bi_{1.8}Pb_{0.4})Sr_2Ca_{2.1-x}Ho_xCu_{3.1}O_{10+\delta}$ with $x=0.000$, 0.025, 0.075, and 0.200. The inset shows the variation of J_c with x.

3. 2 Mechanical measurements

The room temperature Vickers microhardness H_V is calculated for $(Bi_{1.8}Pb_{0.4})Sr_2Ca_{2.1-x}Ho_xCu_{3.1}O_{10+\delta}$ phase according to Eq. (1). H_V values are plotted as a function of the applied loads in Fig. 8 for samples with $x=0.000$, 0.025, 0.075, and 0.200. The measured indentation diagonal length (d) and the calculated Vickers microhardness H_V for all samples are listed in Table 4. It is observed that H_V increases by increasing Ho content from $x=0.000$ to $x=0.025$, and then it has a reverse trend for $x>0.025$. Thus, the low content of partial substitution of Ca^{2+} ions by Ho^{3+} ions has a significant effect on improving the microhardness of (Bi,Pb)-2223 superconducting phase. This improvement can be attributed to the reduction of porosity and the improvement of the weak links between grains. This result is found to be consistent with the obtained SEM micrograph results. The decrease of the measured Vickers microhardness with increasing of Ho content for $x>0.025$ is quite similar to that obtained by

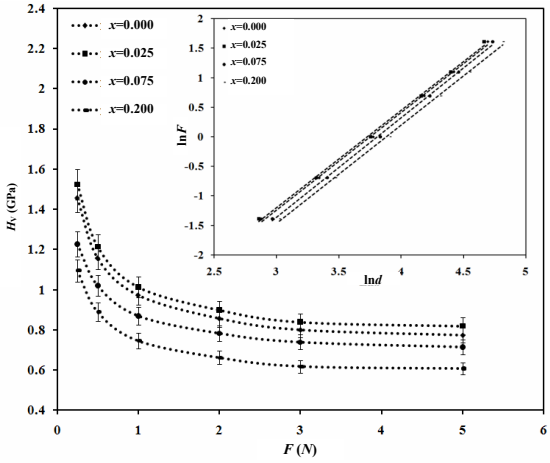

Fig. 8 Dependence of Vickers microhardness H_V on the applied load F for $(Bi_{1.8}Pb_{0.4})Sr_2Ca_{2.1-x}Ho_xCu_{3.1}O_{10+\delta}$ with $x=0.000$, 0.025, 0.075, and 0.200. The inset shows the variation of $\ln H_V$ with $\ln d$ for $(Bi_{1.8}Pb_{0.4})Sr_2Ca_{2.1-x}Ho_xCu_{3.1}O_{10+\delta}$ with $x=0.000$, 0.025, 0.075, and 0.200.

Table 4 Measured diagonal length and calculated microhardness value of BSCCO samples for different applied loads

x	F (N)	H_V (GPa)	d (μm)	x	F (N)	H_V (GPa)	d (μm)
0.000	0.25	1.46	17.84	0.100	0.25	1.21	19.58
	0.50	1.16	28.29		0.50	0.98	30.76
	1.00	0.97	43.63		1.00	0.83	47.30
	2.00	0.86	65.72		2.00	0.74	70.90
	3.00	0.80	83.29		3.00	0.70	89.10
	5.00	0.78	109.36		5.00	0.68	117.00
0.025	0.25	1.52	17.44	0.150	0.25	1.16	19.99
	0.50	1.21	27.63		0.50	0.94	31.41
	1.00	1.01	42.76		1.00	0.79	48.48
	2.00	0.90	64.19		2.00	0.70	72.71
	3.00	0.84	81.38		3.00	0.66	91.75
	5.00	0.82	106.34		5.00	0.64	120.45
0.050	0.25	1.32	18.75	0.200	0.25	1.10	20.57
	0.50	1.08	29.30		0.50	0.89	32.28
	1.00	0.92	44.90		1.00	0.75	49.86
	2.00	0.82	67.06		2.00	0.66	74.85
	3.00	0.78	84.72		3.00	0.62	94.84
	5.00	0.76	110.82		5.00	0.61	123.53
0.075	0.25	1.23	19.44				
	0.50	1.02	30.15				
	1.00	0.87	46.17				
	2.00	0.78	68.80				
	3.00	0.74	86.73				
	5.00	0.72	113.87				

Yilmazlar *et al*. [14] in $Bi_{1.6}Pb_{0.4}Sr_2Ca_{2-x}Sm_xCu_3O_y$ phase. They attributed this behavior to the increase of void density and the resistance to crack propagation. The H_V–F curve behavior shows that the H_V decreases non-linearly as the applied load increases up to 3 N, beyond which the curves tend to attain saturation (nearly plateau) region. This non-linear behavior is also observed for (Bi,Pb)-2223 phase [12–15,30–34] and it is known as indentation size effect (ISE). The ISE behavior can be explained qualitatively on the basis of penetration depth of the indenter. Since the indenter penetrates only surface layers at small applied loads, the surface effect is more pronounced at these loads. However, as the depth of penetration increases, the effect of inner layers becomes more and more prominent, and ultimately there is no change in the values of hardness with applied load [71]. The substantial variation of microhardness is observed with increasing load between 0.25 and 3.00 N. This behavior is due to the contribution of weak grain boundaries and the process of crack formation along grain boundaries [14]. The H_V–F results are analyzed according to different models as follows.

3. 2. 1 Meyer's law

Meyer's law is the most basic method used in describing the ISE behavior [72,73]. It gives a relation between the applied load F and the indentation diagonal length d:

$$F = Ad^n \tag{6}$$

where A is a constant, representing the load needed to initiate unit indentation. The exponent n is called Meyer's index and describes the ISE. The value of n is less than 2 for normal ISE, while for reverse ISE, the value of n is greater than 2. When $n = 2$, H_V is independent of the applied load. The typical plots of the dependence of ln$F$ on ln$d$ for $(Bi_{1.8}Pb_{0.4})Sr_2Ca_{2.1-x}Ho_xCu_{3.1}O_{10+\delta}$, $x = 0.000$, 0.025, 0.075, and 0.200, superconducting samples are shown in the inset of Fig. 8, and the fitting parameters according to Eq. (6) is listed in Table 5. It is obvious from Table 5 that all prepared samples have $n < 2$, indicating a normal ISE behavior. Here the values of A are very small to be acceptable for the ceramic materials which are characterized by their high microhardness. Thus, Meyer's law can explain the ISE behavior of the data qualitatively well, but it cannot determine the true microhardness [34].

3. 2. 2 Hays–Kendall approach

Hays–Kendall (HK) approach displays that there exists a minimum load W (specimen resistance) to initiate plastic deformation below which only elastic deformation is occurred [74]. It is found that indentation size is proportional to an effective load

$F_{\text{eff}} = F - W$ rather than the applied load itself, and the following relationship (modified Kick's law) is proposed:

$$F - W = A_1 d^2 \tag{7}$$

where A_1 is the load independent microhardness constant. The values of W and A_1 are calculated from the linear plotting of F versus d^2 and are also listed in Table 5. Figure 9 shows the variation of F versus d^2 for $(Bi_{1.8}Pb_{0.4})Sr_2Ca_{2.1-x}Ho_xCu_{3.1}O_{10+\delta}$ phase with x = 0.000, 0.025, 0.075, and 0.200. According to the HK approximation, Hays–Kendall microhardness H_{HK} and the Hays–Kendall load independent microhardness H_{HKin} can be calculated by the following equations, respectively:

$$H_{\text{HK}} = 1854.4 \times \frac{F - W}{d^2} \tag{8}$$

$$H_{\text{HKin}} = 1854.4 \times A_1 \tag{9}$$

The values of W are positive for all the samples, meaning that the applied load is sufficient to create both the elastic and the plastic deformation. The calculated values of W are found to be larger than the acceptable values [75]. Similar results were observed by Kölemen *et al*. [32], and they reported that the values of W (0.128–0.163 N) seem to be large to be accepted when studied the effect of partial substitution of Ca^{2+} ions by Sm^{3+} ions on the superconducting properties of $Bi_{1.6}Pb_{0.4}Sr_2Ca_{2-x}Sm_xCu_3O_y$. Similarly, there is reason to believe that W values (0.188–0172 N) obtained in this study seem to be large. Also, according to Ionescu *et al.* [76], Vickers nanoindentation tests were conducted on the similar BSCCO materials and plastic indentation impressions were observed at the load as low as 10 mN. The constant A_1 is suggested to be a measure of the load independent microhardness H_{HKin}, and their values increase as x increases to 0.025 and then decrease for $x > 0.025$, confirming the experimental variation of H_{V} with x.

3. 2. 3 *Elastic/plastic deformation model*

Bull *et al.* [77] proposed that the dependence of indentation size on the applied load can be obtained by way of the equation:

$$F = A_2 (d + d_0)^2 \tag{10}$$

where A_2 is a constant and d_0 is related to d plastic deformation. The values of A_2 and d_0 are calculated from $F^{1/2}$ versus d curves for all the samples and are listed in Table 5. Figure 10 shows the variation of

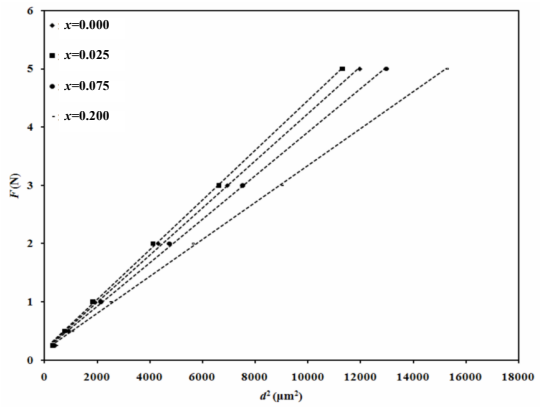

Fig. 9 Variation of the applied load F with d^2 according to Hays–Kendall model for $(Bi_{1.8}Pb_{0.4})Sr_2Ca_{2.1-x}Ho_xCu_{3.1}O_{10+\delta}$ with x = 0.000, 0.025, 0.075, and 0.200.

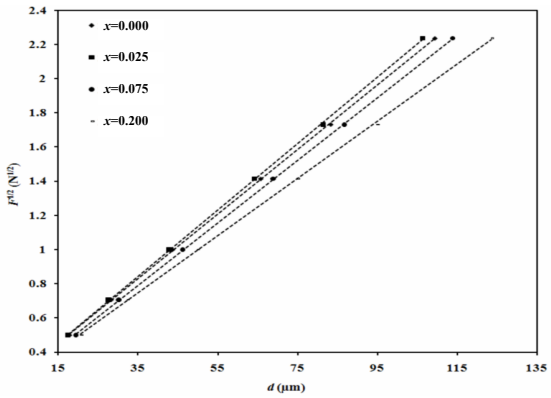

Fig. 10 Plots of $F^{1/2}$ versus d according to elastic/plastic deformation model for $(Bi_{1.8}Pb_{0.4})Sr_2Ca_{2.1-x}Ho_xCu_{3.1}O_{10+\delta}$ with x = 0.000, 0.025, 0.075, and 0.200.

Table 5 Microhardness analysis results of different models for $(Bi_{1.8}Pb_{0.4})Sr_2Ca_{2.1-x}Ho_xCu_{3.1}O_{10+\delta}$ phase

x	Meyer's law		Hays–Kendall model		EPD model		PSR model	
	n	$A\times10^{-3}$ (N/μm^2)	W (N)	$A_1\times10^{-4}$ (N/μm^2)	$A_2\times10^{-4}$ (N/μm^2)	d_0 (μm)	$\alpha\times10^{-3}$ (N/μm)	$\beta\times10^{-4}$ (N/μm^2)
0.000	1.66	2.04	0.188	4.05	3.56	9.02	7.88	3.43
0.025	1.65	2.12	0.179	4.28	3.77	8.56	7.89	3.63
0.050	1.68	1.74	0.168	3.95	3.52	8.19	6.91	3.42
0.075	1.69	1.60	0.169	3.75	3.35	8.25	6.60	3.26
0.100	1.67	1.65	0.172	3.55	3.15	8.85	6.72	3.05
0.150	1.66	1.64	0.178	3.34	2.96	9.43	6.77	2.86
0.200	1.66	1.57	0.172	3.17	2.80	9.63	6.55	2.71

$F^{1/2}$ versus d for $(Bi_{1.8}Pb_{0.4})Sr_2Ca_{2.1-x}Ho_xCu_{3.1}O_{10+\delta}$ phase with $x = 0.000$, 0.025, 0.075, and 0.0200. The elastic/plastic deformation microhardness H_{EPD} and the elastic/plastic deformation load independent microhardness H_{EPDin} are calculated using:

$$H_{EPD} = 1854.4 \times \frac{F}{(d + d_0)^2} \quad (11)$$

$$H_{EPDin} = 1854.4 \times A_2 \quad (12)$$

As seen in Table 5, the value of d_0 is positive for all the samples. This means that, for this range of applied loads, the elastic deformation is observed along with plastic deformation and elastic relaxation is present. The presence of elastic deformation along with plastic deformation is the reason of ISE behavior for our samples. Also, it is found that d_0 changes randomly, and similar behavior was reported by previous studies on BSCCO system [32,33,78]. The constant A_2 is related to load independent hardness H_{EPDin}, and their values increase as x increases to 0.025 and then decrease for $x > 0.025$, confirming the experimental variation of H_V with x.

3. 2. 4 Proportional sample resistance model

Proportional sample resistance (PSR) model which was developed by Li and Bradt [79] is successfully used for the analysis of microhardness of materials showing the ISE behavior. This model is given by the equation:

$$F = \alpha d + \beta d^2 \quad (13)$$

where α is the surface energy, and the change in the α value is associated with the energy dispersion of the surface cracks [31]; β is a parameter used to calculate the real microhardness. According to Eq. (13) the relation between F/d against d yields a straight line with slope corresponding to the parameter β, and the intercept represents the surface energy constant α. Figure 11 represents the variation of F/d against d for $(Bi_{1.8}Pb_{0.4})Sr_2Ca_{2.1-x}Ho_xCu_{3.1}O_{10+\delta}$ phase with $x =$ 0.000, 0.025, 0.075, and 0.200. The calculated values of α and β are listed in Table 5. The value of α is positive for all the samples, consisting with the results obtained from Hays–Kendall approach, where the term αd in the PSR model is equivalent to the constant W in Hays–Kendall approach. It is clear that the value of α increases by increasing Ho content to $x = 0.025$ and then it has a reverse trend. The enhancement can be ascribed to the dissipation of the cracks at the interfaces [80]. Moreover, the constant β is suggested to be a measure of the load independent microhardness H_{PSRin} according to Eq. (15). It is noted that the values of β and H_{PSRin} confirm the experimental variation of H_V with x. Based on PSR model, PSR microhardness H_{PSR} and the PSR load independent microhardness H_{PSRin} are given by the following equations, respectively:

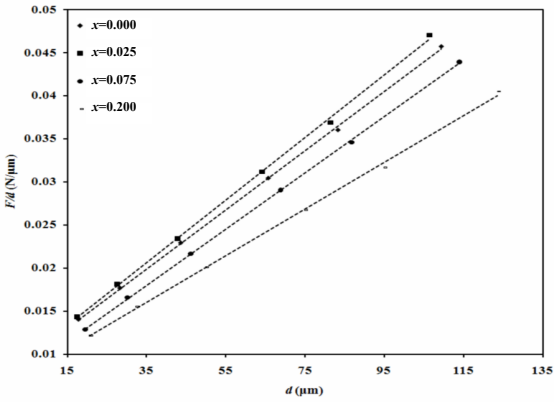

Fig. 11 Plots of F/d versus d according to proportional sample resistance model for $(Bi_{1.8}Pb_{0.4})Sr_2Ca_{2.1-x}Ho_xCu_{3.1}O_{10+\delta}$ with $x = 0.000$, 0.025, 0.075, and 0.200.

$$H_{PSR} = 1854.4 \times \frac{\alpha_1 d + \beta d^2}{d^2} \quad (14)$$

$$H_{PSRin} = 1854.4 \times \beta \quad (15)$$

In order to determine the consistency of the above mentioned models with our samples, the experimental and calculated microhardness at the plateau region as well as the load independent microhardness values according to each model are listed in Table 6. It is obvious from Table 6 that the true microhardness value according to the HK model (0.751 GPa) of the sample with $x = 0.000$ is lower than the hardness value in the plateau region ($H_V = 0.802 - 0.775$ GPa). This behavior is also observed in all the other samples. Although the HK model has been applied to BSCCO system in Refs. [34,81,82] for example, the consistency is not very good in our case; it is found that W seems to be large to be accepted, and the values of the true hardness calculated by this model are not in the plateau region. Therefore, one can conclude that HK approach is not suitable for describing our experimental data. Similar behavior of failure of HK model in BSCCO system was observed in many previous works [14,32,33,75, 76,78]. While, for EPD model, it is found that d_0 changes randomly, and the values of the true hardness

calculated by this model are not in the plateau region. One can conclude that EPD approach is not suitable for describing our experimental data either. Finally, PSR model is determined as the most successful model describing the mechanical properties of our samples. Similar behavior was observed by Khalil [83] studying the influence of isothermal hot pressing–doping treatment on the microstructure, electrical, and mechanical properties of $Bi_2Sr_{3-x}Ca_xCu_2O_{8+\delta}$ bulk samples. Also, to confirm PSR model is the best model, the deviation percentages between the experimental and theoretical true microhardness with x according to each model are calculated for $(Bi_{1.8}Pb_{0.4})Sr_2Ca_{2.1-x}Ho_xCu_{3.1}O_{10+\delta}$ phase and their values are listed in Table 7. It can be seen that the deviation percentages between the experimental true microhardness and the theoretical ones obtained from PSR model are very low in comparison with the other deviation percentages obtained from the other models. In addition, Figs. 12–15 show a comparison between the experimental H_V and theoretical values calculated according to different models for $(Bi_{1.8}Pb_{0.4})Sr_2Ca_{2.1-x}Ho_xCu_{3.1}O_{10+\delta}$ phase with $x = 0.000$, 0.025, 0.100, and 0.200. From these figures, it is clear that the experimental true microhardness values, for all the samples, are very close to those obtained from the PSR model, followed by Hays–Kendall model. However, the values of the EPD model are found to be very far from the experimental true microhardness values. Therefore, it could be concluded that the results of the PSR model are consistent with our load independent microhardness values which can give a good explanation for the true microhardness of the studied samples.

Table 6 Variation of the experimental and calculated microhardness at the plateau region, and the load independent microhardness according to HK, EPD, and PSR models versus the substitution content for $(Bi_{1.8}Pb_{0.4})Sr_2Ca_{2.1-x}Ho_xCu_{3.1}O_{10+\delta}$ phase

x	H_V in plateau region (GPa)	Hays–Kendall model		EPD model		PSR model	
		H_{HK} (GPa)	H_{HKin} (GPa)	H_{EPD} (GPa)	H_{EPDin} (GPa)	H_{PSR} (GPa)	H_{PSRin} (GPa)
0.000	0.802–0.775	0.752–0.746	0.751	0.653–0.662	0.660	0.812–0.770	0.637
0.025	0.840–0.820	0.790–0.791	0.793	0.688–0.702	0.698	0.854–0.812	0.674
0.050	0.775–0.755	0.732–0.730	0.733	0.644–0.655	0.652	0.785–0.750	0.634
0.075	0.740–0.715	0.698–0.691	0.695	0.617–0.622	0.621	0.746–0.712	0.605
0.100	0.701–0.677	0.661–0.654	0.658	0.580–0.585	0.584	0.706–0.673	0.566
0.150	0.661–0.639	0.622–0.616	0.620	0.543–0.550	0.548	0.668–0.635	0.531
0.200	0.619–0.608	0.583–0.587	0.588	0.510–0.523	0.519	0.630–0.601	0.502

Table 7 Percentage deviation from the measured Vickers microhardness according to different models for $(Bi_{1.8}Pb_{0.4})Sr_2Ca_{2.1-x}Ho_xCu_{3.1}O_{10+\delta}$ phase (Unit: %)

x	Model	F (N)					
		0.25	0.50	1.00	2.00	3.00	5.00
0.000	HK	75.34	37.67	18.83	9.42	6.28	3.77
	EPD	126.72	73.94	45.62	29.33	22.83	17.18
	PSR	0.10	0.47	0.28	–0.03	–1.23	0.66
0.025	HK	71.68	35.84	17.92	8.96	5.97	3.58
	EPD	122.35	71.59	44.06	28.46	22.15	16.76
	PSR	0.74	0.88	–0.23	–0.23	–1.63	1.02
0.050	HK	67.23	33.61	16.81	8.40	5.60	3.36
	EPD	106.40	63.69	39.80	25.91	20.26	15.32
	PSR	0.09	0.80	0.06	–0.06	–1.30	0.72
0.075	HK	67.23	33.61	16.81	8.40	5.60	3.36
	EPD	101.98	61.68	38.61	25.22	19.77	14.90
	PSR	–0.56	0.94	0.03	0.12	–0.85	0.40
0.100	HK	68.69	34.34	17.17	8.59	5.72	3.43
	EPD	110.75	65.79	40.90	26.51	20.84	15.69
	PSR	0.47	0.84	–0.16	–0.59	–0.79	0.64
0.150	HK	71.36	35.68	17.84	8.92	5.95	3.57
	EPD	116.63	69.10	42.71	27.63	21.62	16.28
	PSR	0.06	1.00	–0.10	–0.28	–1.02	0.65
0.200	HK	68.77	34.38	17.19	8.60	5.73	3.44
	EPD	115.54	68.56	42.35	27.38	21.33	16.20
	PSR	0.30	1.31	0.02	–0.38	–1.88	1.17

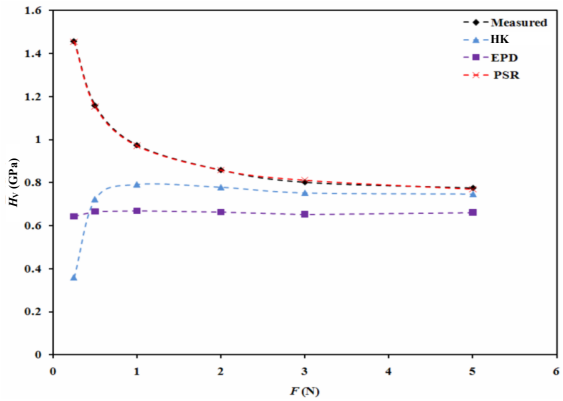

Fig. 12 Variation of the measured H_V and calculated H_V according to different models with the applied load for $(Bi_{1.8}Pb_{0.4})Sr_{1.9}Ca_{2.1}Cu_{3.1}O_{10+\delta}$ phase.

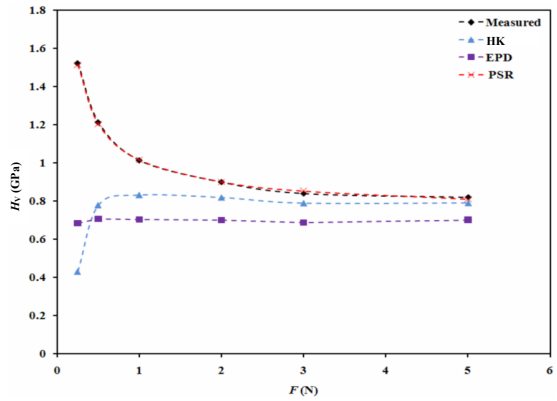

Fig. 13 Variation of the measured H_V and calculated H_V according to different models with the applied load for $(Bi_{1.8}Pb_{0.4})Sr_2Ca_{2.075}Ho_{0.025}Cu_{3.1}O_{10+\delta}$ phase.

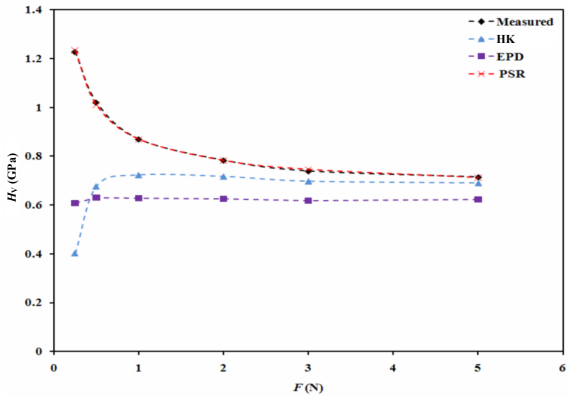

Fig. 14 Variation of the measured H_V and calculated H_V according to different models with the applied load for $(Bi_{1.8}Pb_{0.4})Sr_2Ca_2Ho_{0.1}Cu_{3.1}O_{10+\delta}$ phase.

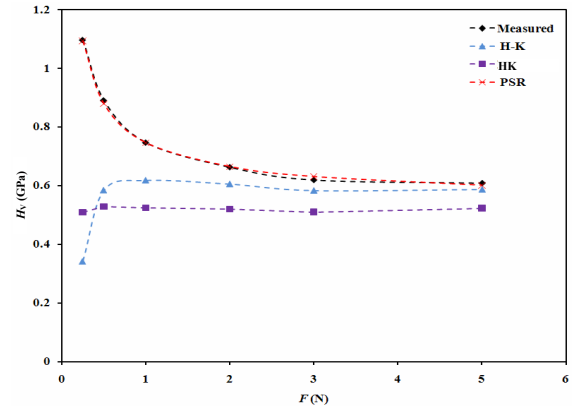

Fig. 15 Variation of the measured H_V and calculated H_V according to different models with the applied load for $(Bi_{1.8}Pb_{0.4})Sr_{1.9}Ca_{1.9}Ho_{0.2}Cu_{3.1}O_{10+\delta}$ phase.

4 Conclusions

A series of $(Bi_{1.8}Pb_{0.4})Sr_2Ca_{2.1-x}Ho_xCu_{3.1}O_{10+\delta}$ samples with $x = 0.000$, 0.025, 0.050, 0.075, 0.100, 0.150, and 0.200 were successfully prepared via conventional solid-state reaction technique. The experimental results showed that Ho substitution at very low percentages ($0.000 < x \leqslant 0.025$) enhanced the volume fraction of the (Bi,Pb)-2223 phase, T_c, and J_c. While the values of T_c and J_c were decreased by increasing the Ho content up to $x = 0.200$ due to the formation of weak links. Moreover, the solubility limit of Ho substituted in (Bi,Pb)-2223 system was higher than that reported for the other rare-earth elements and was less detrimental to the superconductivity. The analysis of electrical resistivity according to the bipolaron model showed that the number of localized carriers and boson–boson relaxation time decreased, while the scattering cross-section increased by increasing Ho contents up to $x = 0.025$. This result confirmed the increase in T_c at $x = 0.025$. By distinguishing the contrast of T_c and T^* versus Ho content, it can be concluded that transport properties is determined by the spin fluctuation scattering. Finally, the Vickers microhardness results indicated that H_V increased as x increased from 0.000 to 0.025 and it had a normal ISE behavior. The results of the microhardness were examined using different models such as Meyer's law, Hays–Kendall approach, elastic/plastic deformation model, and PSR model. The PSR model was found to be the most successful model describing the mechanical properties of the studied samples.

Acknowledgements

This work was performed in the Superconductivity and Metallic Glass Lab, Physics Department, Faculty of Science, Alexandria University, Alexandria, Egypt.

References

[1] Bilgili O, Kocabaş K. Effects of Gd substitution on magnetic, structural and superconducting properties of $Bi_{1.7-x}Pb_{0.3}Gd_xSr_2Ca_2Cu_3O_y$. *J Mater Sci: Mater El* 2015, **26**: 1700–1708.

[2] Erdem M, Özturk Ö, Yucel E, *et al*. Effect of Gd addition on the activation energies of Bi-2223 superconductor. *Physica B* 2011, **406**: 705–709.

[3] Özkurt B, Madre MA, Sotelo A, *et al*. Relationship between growth speed, microstructure, mechanical and electrical properties in Bi-2212/Ag textured composites. *J Supercond Nov Magn* 2012, **25**: 799–804.

[4] Gündoğmuş H, Özçelik B, Özkurt B, *et al*. Physical, mechanical and magnetic properties of the Yb-substituted $Bi_2Sr_2Ca_1Cu_2O_y$ textured superconductor. *J Supercond Nov Magn* 2013, **26**: 111–115.

[5] Bal S, Dogruer M, Yildirim G, *et al*. Role of cerium addition on structural and superconducting properties of Bi-2212 system. *J Supercond Nov Magn* 2012, **25**: 847–856.

[6] Zargar Shoushtari M, Mousavi Ghahfarokhi SE. A study of the magnetic properties of $Bi_{1.64-x}Pb_{0.36}Cd_xSr_2Ca_2Cu_3O_y$ superconductor. *J Supercond Nov Magn* 2011, **24**: 1505–1511.

[7] Abou-Aly AI, Abdel Gawad MMH, Awad R, *et al*. Improving the physical properties of (Bi,Pb)-2223 phase by SnO_2 nano-particles addition. *J Supercond Nov Magn* 2011, **24**: 2077–2084.

[8] Yildirim G, Bal S, Yucel E, *et al*. Effect of Mn addition on structural and superconducting properties of (Bi,Pb)-2223 superconducting ceramics. *J Supercond Nov Magn* 2012, **25**: 381–390.

[9] Sarun PM, Vinu S, Shabna R, *et al*. Properties of superconducting, polycrystalline dysprosium-doped $Bi_{1.6}Pb_{0.5}Sr_{2-x}Dy_xCa_{1.1}Cu_{2.1}O_{8+\delta}$ ($0 \leqslant x \leqslant 0.5$). *Mater Res Bull* 2009, **44**: 1017–1021.

[10] Sedky A. The impact of Y substitution on the 110 K high T_c phase in a Bi(Pb):2223 superconductor. *J Phys Chem Solids* 2009, **70**: 483–488.

[11] Mihalache V, Deac IG, Pop AV, *et al*. The pinning force density in polycrystalline $Bi_{1.8}Pb_{0.4}Sr_2Ca_{2-x}Y_xCu_3O_y$ multiphase systems. *Curr Appl Phys* 2011, **11**: 1010–1014.

[12] Marconi D, Stiufiuc G, Pop AV. Effect of partial substitution of Ca by 4f elements on dissipative processes in Bi:2223 superconductors. *Journal of Physics Conference Series* 2009, **153**: 012022.

[13] Terzioglu C, Yilmazlar M, Ozturk O, *et al*. Structural and physical properties of Sm-doped $Bi_{1.6}Pb_{0.4}Sr_2Ca_{2-x}Sm_xCu_3O_y$ superconductors. *Physica C* 2005, **423**: 119–126.

[14] Yilmazlar M, Cetinkara HA, Nursoy M, *et al*. Thermal expansion and Vickers hardness measurements on $Bi_{1.6}Pb_{0.4}Sr_2Ca_{2-x}Sm_xCu_3O_y$ superconductors. *Physica C* 2006, **442**: 101–107.

[15] Görür O, Küçükömeroğlu T, Terzioğlu C, *et al*. The effect of Ag diffusion on properties of $YBa_2Cu_3O_{7-x}$ thin films produced by electron beam deposition techniques. *Physica C* 2005 **418**: 35–42.

[16] Hawa JS, Azhan H, Yahya SY, *et al*. The effect of Eu substitution onto Ca site in Bi(Pb)-2223 superconductor via co-precipitation method. *J Supercond Nov Magn* 2013, **26**: 979–983.

[17] Alexandrov AS, Zavaritsky VN, Dzhumanov S. Hall effect and resistivity in underdoped cuprates. *Phys Rev B* 2004, **69**: 052505.

[18] Alexandrov AS, Mott NF. Lattice and spin bipolarons in metal oxides and doped fullerenes. *J Supercond* 1994, **7**: 599–605.

[19] Alexandrov AS. Critical temperature of high-T_c superconductors in the bipolaron model. *AIP Conf Proc* 2003, **695**: 42.

[20] Hague JP, Kornilovitch PE, Alexandrov AS. Trapping of lattice polarons by impurities. *Phys Rev B* 2008 **78**: 092302.

[21] Aghabagheri S, Mohammadizadeh MR. The bipolaron model in the normal state of Pr-doped $GdBa_2Cu_3O_7$ superconductors. *Supercond Sci Tech* 2010, **23**: 045003.

[22] Sadovskii MV. Pseudogap in high-temperature superconductors. *Physics-Uspekhi* 2001, **44**: 515.

[23] Xu S, Wu XS, Liu G, *et al*. Structure and spin gap in $YBa_2Cu_{3-x}Gd_xO_{7-\delta}$ superconductors. *Physica C* 2004, **417**: 63–68.

[24] Mohammadizadeh MR, Akhavan M. Pseudogap in Gd-based 123 HTSC. *Physica B* 2003, **336**: 410–419.

[25] Naqib SH, Cooper JR, Tallon JL, *et al*. Doping phase diagram of $Y_{1-x}Ca_xBa_2(Cu_{1-y}Zn_y)_3O_{7-\delta}$ from transport measurements: Tracking the pseudogap below T_c. *Phys Rev B* 2005, **71**: 054502.

[26] Prokof'ev DD, Volkov MP, Boikov YA. Pseudogap and its temperature dependence in YBCO from the data of resistance measurements. *Phys Solid State+* 2003, **45**: 1223–1232.

[27] Babaev E, Kleinert H. Nonperturbative XY-model approach to strong coupling superconductivity in two and three dimensions. *Phys Rev B* 1999, **59**: 12083.

[28] Awad R, Abou-Aly AI, Abdel Gawad MMH, *et al*. The influence of SnO_2 nano-particles addition on the Vickers microhardness of (Bi,Pb)-2223 superconducting phase. *J Supercond Nov Magn* 2012, **25**: 739–745.

[29] Awad R, Abou Aly AI, Kamal M, *et al*. Mechanical properties of $(Cu_{0.5}Tl_{0.5})$-1223 substituted by Pr. *J Supercond Nov Magn* 2011, **24**: 1947–1956.

[30] Mohammed NH, Abou-Aly AI, Ibrahim IH, *et al*. Effect of nano-oxides addition on the mechanical properties of $(Cu_{0.5}Tl_{0.5})$-1223 phase. *J Supercond Nov Magn* 2011, **24**: 1463–1472.

[31] Abdeen W, Mohammed NH, Awad R, *et al*. Influence of nano-Ag addition on the mechanical properties of $(Cu_{0.5}Tl_{0.5})$-1223 superconducting phase. *J Supercond Nov Magn* 2013, **26**: 3235–3245.

[32] Kölemen U, Uzun O, Yılmazlar M, *et al*. Hardness and microstructural analysis of $Bi_{1.6}Pb_{0.4}Sr_2Ca_{2-x}Sm_xCu_3O_y$ polycrystalline superconductors. *J Alloys Compd* 2006, **415**: 300–306.

[33] Aydin H, Cakiroglu O, Nursoy M, *et al*. Mechanical and superconducting properties of the $Bi_{1.8}Pb_{0.35}Sr_{1.9}Ca_{2.1}Cu_3Gd_xO_y$ system. *Chin J Phys* 2009, **47**: 192–206.

[34] Terzioglu C. Investigation of some physical properties of Gd added Bi-2223 superconductors. *J Alloys Compd* 2011, **509**: 87–93.

[35] Mohammed NH, Awad R, Abou-Aly AI, *et al*. Optimizing the preparation conditions of Bi-2223 superconducting phase using PbO and PbO_2. *Materials Sciences and Applications* 2012, **3**: 224–233.

[36] Leenders A, Mich M, Freyhard HC. Influence of thermal cycling on the mechanical properties of VGF melt-textured YBCO. *Physica C* 1997, **279**: 173–180.

[37] Abou-Aly AI, Awad R, Mahmoud SA, *et al*. EPR studies of (Bi,Pb)-2223 phase substituted by Ruthenium ions. *J Alloys Compd* 2011, **509**: 7381–7388.

[38] Nursoy M, Yilmazlar M, Terziogl C, *et al*. Transport, microstructure and mechanical properties of Au diffusion-doped Bi-2223 superconductors. *J Alloys Compd* 2008, **459**: 399–406.

[39] Terzioglu C, Aydin H, Ozturk O, *et al*. The influence of Gd addition on microstructure and transport properties of Bi-2223. *Physica B* 2008, **403**: 3354–3359.

[40] Pu MH, Song WH, Zhao B, *et al*. Enhanced flux pinning in (Bi,Pb)-2223/Ag tapes by slight Pr-doping. *Physica C* 2001, **361**: 181–188.

[41] Koyama S, Endo U, Kawai T. Preparation of single 110 K phase of the Bi–Pb–Sr–Ca–Cu–O superconductor. *Japanese Journal of Applied Physics* 1988, **27**: L1861–L1863.

[42] Abou-Aly AI, Mahmoud SA, Awad R, *et al*. Electrical resistivity and magnetoresistance studies of (Bi,Pb)-2223 phase substituted by Ru. *J Supercond Nov Magn* 2010, **23**: 1575–1588.

[43] Kocabaş K, Şakiroğlu S, Çiftçioğlu M, *et al*. The effect of Zn substitution of Ca in BiPbSrCaCuO superconductors sintered at 830 ℃. *J Supercond Nov Magn* 2009, **22**: 749–754.

[44] Özkurt B. The effects of yttrium substitution in Bi-2223 superconductors. *J Mater Sci: Mater El* 2013, **24**: 758–763.

[45] Shannon RD. Revised effective ionic radii and systematic studies of interatomic distances in halides and chalcogenides. *Acta Cryst* 1976, **A32**: 751–767.

[46] Ozturk O, Akdogan M, Aydin H, *et al*. Substitution of Sm at Ca site in $Bi_{1.6}Pb_{0.4}Sr_2Ca_{2-x}Sm_xCu_3O_y$ superconductors. *Physica B* 2007, **399**: 94–100.

[47] Xiong YM, Li L, Luo XG, *et al*. Transport properties of Ru-doped $La_{1.85}Sr_{0.15}CuO_4$ and the effect of carrier concentration compensation. *J Phys: Condens Matter* 2003, **15**: 1693–1704.

[48] Aksan MA, Yakinci ME, Kadowaki K. The effect of Ru substitution on the thermal, structural and magnetic properties of $Bi_3Sr_2Ca_2Cu_3O_\delta$ superconducting system. *J Supercond Nov Magn* 2010, **23**: 371–380.

[49] Bilgili O, Selamet Y, Kocabaş K. Effects of Li substitution in Bi-2223 superconductors. *J Supercond Nov Magn* 2008, **21**: 439–449.

[50] Anis-ur-Rehman M, Mubeen M. Synthesis and enhancement of current density in cerium doped Bi(Pb)Sr(Ba)-2223 high T_c superconductor. *Synthetic Metals* 2012, **162**: 1769–1774.

[51] Anderson PW. Hall effect in the two-dimensional Luttinger liquid. *Phys Rev Lett* 1991, **67**: 2092.

[52] Abou Aly AI, Ibrahim IH, Awad R, *et al*. Stabilization of Tl-1223 phase by arsenic substitution. *J Supercond Nov Magn* 2010, **23**: 1325–1332.

[53] Koo JH, Cho G. The spin-gap in high *T*-c superconductivity. *J Phys: Condens Matter* 2003, **15**: L729–L733.

[54] Kameli P, Salamati H, Abdolhosseini I, *et al*. Thermally activated flux creep in the $Bi_{1.66}Pb_{0.34}Sr_2Ca_{2-x}Mg_xCu_3O_y$ superconductors. *Physica C* 2008, **468**: 137–141.

[55] Laximi Narasaiah E, Subba Rao UV, Pena O, *et al*. Annealing effects on T_c in $Bi_2Sr_2Ca_{0.9}Y_{0.1}Cu_2O_{8+\delta}$ system. *Mat Sci Eng B* 1992, **15**: 37–39.

[56] Abrikosov AA, Gor'kov LP. Contribution to the theory of superconducting alloys with paramagnetic impurities. *Sov Phys JETP* 1961, **12**: 1243.

[57] Vélez M, Cyrille MC, Kim S, *et al*. Enhancement of superconductivity by decreased magnetic spin-flip scattering: Nonmonotonic T_c dependence with enhanced magnetic ordering. *Phys Rev B* 1999, **59**: 14659.

[58] Nanda Kishore K, Satyavathi S, Muralidhar M, *et al*. Thermoelectric power studies on the Sm substituted BPSCCO (2223) superconductors. *Physica C* 1995, **252**: 49–53.

[59] Singh R, Gupta A, Agarwal SK, *et al*. Superconductivity in Pr-doped $Bi_2Ca_2Sr_2Cu_3O_y$. *Supercond Sci Technol* 1998, **11**: 311–314.

[60] Kothawale RR, Dole BN, Shah SS. Effect of substitution of Ce on superconducting properties of $Bi_{1.7}Pb_{0.3}Sr_2Ca_{2-x}Ce_xCu_3O_{10+\delta}$ system. *Pramana* 2002, **58**: 871–875.

[61] Aliabadi A, Akhavan Farshchi Y, Akhavan M. A new Y-based HTSC with T_c above 100 K. *Physica C* 2009, **469**: 2012–2014.

[62] Alexandrov AS, Bratkovsky AM, Mott NF. Hall-effect and resistivity of high-*T*(c) oxides in the bipolaron model. *Phys Rev Lett* 1994, **72**: 1734–1737.

[63] Esmaeili A, Sedghi H, Golzan MM, *et al*. The normal state properties of $Y_3Ba_5Cu_{8-x}Zn_xO_{18-\delta}$ superconductor in bipolaron model. *J Supercond Nov Magn* 2011, **24**: 2237–2242.

[64] Fukuyama H, Kohno H. The spin gap and extended *t*–*J* model. *Physica C* 1997, **282–287**: 124–127.

[65] Lee PA. Gauge field, Aharonov–Bohm flux, and high-T_c

superconductivity. *Phys Rev Lett* 1989, **63**: 680.

[66] Katona TM, Pierson SW. Zero-field current–voltage characteristics in high-temperature superconductors. *Physica C* 1996, **270**: 242–248.

[67] Repaci JM, Kwon C, Jiang XG, *et al*. Absence of Kosterlitz–Thouless transition in ultra-thin YBCO films. *Bulletin of the American Physical Society* 1995, **40**: 445.

[68] Díaz A, Mechin L, Berghuis P, *et al*. Observation of viscous flux flow in $YBa_2Cu_3O_{7-\delta}$ low-angle grain boundaries. *Phys Rev B* 1998, **58**: R2960(R).

[69] Kwak JF, Venturini EL, Ginley DS, *et al*. Grain decoupling at low magnetic fields in ceramic $YBa_2Cu_3O_{7-\delta}$. In: *Novel Superconductivity*. Wolf SA, Kresin VZ, Eds. New York: Plenum Press, 1987: 983–991.

[70] Aloysius RP, Guruswamy P, Syamaprasad U. Enhanced flux pinning in (Bi,Pb)-2223 superconductor by Nd addition. *Supercond Sci Tech* 2005, **18**: 427–431.

[71] Foerster CE, Lima E, Rodrigues Jr. P, *et al*. Mechanical properties of Ag-doped top-seeded melt-grown YBCO pellets. *Braz J Phys* 2008, **38**: 341–345.

[72] Sangwal K, Surowska B. Study of indentation size effect and microhardness of $SrLaAlO_4$ and $SrLaGaO_4$ single crystals. *Mater Res Innov* 2003, **7**: 91–104.

[73] Tickoo R, Tandon RP, Bamzai KK, *et al*. Microindentation studies on samarium-modified lead titanate ceramics. *Mater Chem Phys* 2003, **80**: 446–451.

[74] Hays C, Kendall EG. An analysis of Knoop microhardness. *Metallography* 1973, **6**: 275–282.

[75] Peng Z, Gong J, Miao H. On the description of indentation size effect in hardness testing for ceramics: Analysis of the nanoindentation data. *J Eur Ceram Soc* 2004, **24**: 2193–2201.

[76] Ionescu M, Zeimetz B, Dou SX. Microhardness anisotropy of Bi-2212 crystals. *Physica C* 1998, **306**: 213–217.

[77] Bull SJ, Page TF, Yoffe EH. An explanation of the indentation size effect in ceramics. *Phil Mag Lett* 1989, **59**: 281–288.

[78] Ozturk O. Some physical properties and Vickers hardness measurements of Fe diffusion-doped $Bi_{1.8}Pb_{0.35}Sr_{1.9}Ca_{2.1}Cu_3O_y$ superconductors. *J Mater Sci: Mater El* 2012, **23**: 1235–1242.

[79] Li H, Bradt RC. The microhardness indentation load/size effect in rutile and cassiterite single crystals. *J Mater Sci* 1993, **28**: 917–926.

[80] Bobrov VS. Deformation, structure and properties of ceramics and crystals of high-T_c superconductors. *Mat Sci Eng A* 1993, **164**: 146–152.

[81] Ozturk O, Erdem M, Asikuzun E, *et al*. Investigation of indentation size effect (ISE) and micro-mechanical properties of Lu added $Bi_2Sr_2CaCu_2O_y$ ceramic superconductors. *J Mater Sci: Mater El* 2013, **24**: 230–238.

[82] Koralay H, Arslan A, Cavdar S, *et al*. Structural and mechanical characterization of $Bi_{1.75}Pb_{0.25}Sr_2Ca_2Cu_{3-x}Sn_xO_{10+y}$ superconductor ceramics using Vickers microhardness test. *J Mater Sci: Mater El* 2013, **24**: 4270–4278.

[83] Khalil SM. Influence of isothermal hot pressing-doping treatment on the electrical and mechanical properties of bulk Bi–Sr–Ca–Cu–O. *AIP Advances* 2012, **2**: 042183.